Asian Journal of Chemistry; Vol. 36, No. 8 (2024), 1840-1852

ASIAN JOURNAL OF CHEMISTRY

https://doi.org/10.14233/ajchem.2024.31895

Enhanced Photocatalytic Methylene Blue Degradation and Chromium(VI) Photoreduction under Sunlight by Fe_3O_4@rGO@CeO_2/Nd_2O_3 as Magnetic Recyclable Photocatalyst

VISHAL A. NAIK[1,2] and VIKAS A. THAKUR[1,*]

[1]Department of Chemistry, Karmaveer Bhaurao Patil College, Vashi, Navi Mumbai-400703, India
[2]Department of Chemistry, Mahatma Phule ASC College, Panvel, Navi Mumbai-410206, India

*Corresponding author: E-mail: thakur.vikasanant@gmail.com

Received: 6 May 2024; *Accepted*: 7 June 2024; *Published online*: 25 July 2024; AJC-21705

A significant global concern is in the easy separation, recyclability and reusability of photocatalysts in industrial wastewater treatment applications. Therefore, in this study, the synthesis of magnetically separatable Fe_3O_4@rGO@CeO_2/Nd_2O_3 photocatalyst using a one-step solvothermal method is reported, which overcomes all these challenges. A binary lanthanide oxides CeO_2/Nd_2O_3 anchored on rGO-wrapped Fe_3O_4 core-shell magnetic nanoparticles. The synthesized magnetic photocatalyst nanocomposite has been characterized using XRD, FESEM, EDX, HRTEM, TGA-DTA-DSC, VSM, FTIR and UV-visible spectrophotometer. In this work, the Fe_3O_4 synthesized by solvothermal technique achieved the highest saturation magnetization (MS), 101.84 emu/g. The results showed that Fe_3O_4@rGO@CeO_2/Nd_2O_3 photocatalyst had more excellent stability up to 880 ºC confirmed by TGA-DTA-DSC analysis and efficient potential for the degradation of methylene blue by photo-Fenton reaction and reduction of Cr(VI) in formic acid under sunlight. The prepared photocatalyst efficiently degrades 98% of methylene blue in 50 min at neutral pH and quick photoreduction of Cr(VI) of 99% takes place within 40 min. After six cycles, the repeatability of the photocatalytic activity exhibited just a slight reduction in catalytic efficiency for degradation of methylene blue and photoreduction of Cr(VI).

Keywords: Solvothermal synthesis, Lanthanide oxide nanocomposites, Magnetic photocatalyst, Photo-Fenton method.

INTRODUCTION

Over the past few decades, rapid global industrialization has led to severe contamination of aquatic ecosystems and other environments worldwide. The pollutants accumulated in wastewater from the textile, dyeing, leather, pharmaceutical, paper, cosmetics, plastic and synthetic detergent sectors are persistent, environmentally hazardous, non-biodegradable, potentially carcinogenic and highly stable [1]. They include heavy toxic metals, synthetic dyes and synthetic detergents [2]. Synthetic dyes with a concentration ranging from 10 to 200 mg L^{-1} present in wastewater are supposed to be carcinogenic. Humans, plants, microorganisms and animals are exposed to approximately 500 times more hexavalent chromium than trivalent chromium [3]. Chromium finds applications beyond its evident applications in leather tanning and electroplating to encompass ceramics, pigment manufacturing and the paper industry. Extremely toxic, the chromate anion of hexavalent chromium is capable of inducing cancer and mutations in humans [4,5]. The World Health Organization (WHO) advises that the maximum permissible concentration of Cr(VI) in effluent is 0.05 mg L^{-1} [6]. Limited quantities of Cr(III) are essential for the metabolic processes of lipids, carbohydrates and sugars in animals and humans [7,8]. However, excessive concentrations of Cr(III) have been demonstrated to induce harm to the kidneys and liver owing to their propensity for unrestricted diffusion across cellular membranes and their elevated oxidation potential [5,9]. Thus, effluent treatment, refining and recycling are essential for environmental and industrial pollution control.

To eliminate and degrade organic compounds from industrial wastewater, numerous conventional processes have been implemented, including ozonation, precipitation, chemical oxidation, ion-exchange, adsorption, reverse osmosis, biodegradation, flocculation-coagulation, electrocoagulation and others [10,11]. In addition, numerous cost-effective techniques for

the removal of organic pollutants and the efficient reduction of Cr(VI) to Cr(III) have been developed [12-14]. In recent times, advanced oxygen processes (AOPs) have emerged as the predominant method for removal of pigment from water [15]. The most prominent among these methods is the *in situ* photochemical degradation of dyes, which produces an oxidizing agent in water. Several advantages distinguish photocatalytic degradation of dyes over alternative processes, including the almost elimination of secondary pollution and the degradation of pollutants. The photo-Fenton process, which generates hydroxyl radicals ($OH^{\bullet}$) by the decomposition of H_2O_2 in the presence of ferrous ions, is among the most economical AOPs [16-21].

Lanthanide oxides consisting of CeO_2 and Nd_2O_3 are environmental friendly, photocatalytically active and possess low toxicity. CeO_2 nanoparticles have garnered considerable attention due to their unique characteristics, such as thermal stability and n-type semiconductors with a band gap of 3.0 eV. The oxidation state transition of Ce^{3+} to Ce^{4+} and oxygen vacancies are essential for the catalytic activity of CeO_2 [22]. Combined with additional nanoparticles, these defect sites promote enhanced photocatalytic degradation efficiency in both the ultraviolet and visible regions, thereby minimizing electron-hole pair recombination. The efficiency of photocatalytic activity of lanthanide oxide nanocomposites has been demonstrated several times. For example, Munawar *et al.* [23] synthesized a Z-scheme ZnO-Er_2O_3-Nd_2O_3@rGO heterostructure nanocomposite for efficient methylene blue degradation and also evaluated its antibacterial activity. Under the UV light irradiation, Arunpandian *et al.* [11] examined the photocatalytic efficiency of Nd_2O_3/ZnO-GO for the degradation of ciprofloxacin and methylene blue dye. As a magnetic photocatalyst, Subhan *et al.* [24] synthesized a La_2O_3-Fe_3O_4-ZnO nanocomposite that efficiently degrades methyl violet 6B when exposed to visible light. Another type of lanthanide oxide nanocomposites, Byrappa *et al.* [25] developed Bi_2O_3-CeO_2-ZnO photocatalyst as photocatalytic material for degradation of rhodamine B dye. The antibacterial activity [26], electrochemical reduction [27] and nuclear waste immobilization [28] are a few of the applications of the binary nanocomposite CeO_2/Nd_2O_3, which has been synthesized *via* a variety of methods except the solvothermal process [28-30]. However, its photocatalytic methylene blue degradation and hexavalent chromium reduction have yet to be reported.

The rapid loss of suspended catalyst particles during photocatalytic reaction and separation restricts the photocatalytic performance of these composites. These limitations contaminate treated water and increase industrial expenses [31]. The issues may be resolved using magnetically permeable nuclei and catalytically active outer shells. Incorporating magnetic nanoparticles into these materials may enable them to combine catalytic activity with simple separation [31,32]. Fe_3O_4 is an exceptionally auspicious magnetic nanoparticle for incorporation into magnetic nanocomposites. Due to its high saturation magnetization, it is responsive to magnetic fields. For such applications, Fe_3O_4 is more desirable due to its reduced toxicity. Graphene oxide has numerous applications due to its exceptional thermal and mechanical stability, charge transfer-based electrical conductivity and photocatalytic activity when combined with Fe_3O_4. Several attempts have been made to manage electron-hole recombination, which has resulted in improvements in the recyclability of photocatalyst as well as their photocatalytic activity and stability. To enhance the photodegradation of methylene blue and increase the conversion of Fe^{3+} to Fe^{2+}, Yang *et al.* [33] synthesized TiO_2 nanoparticles mounted on reduced graphene oxide (rGO)-wrapped Fe_3O_4 spheres (Fe_3O_4@rGO@TiO_2).

In this study, a magnetic photocatalyst nanocomposite Fe_3O_4@rGO@CeO_2/Nd_2O_3 was synthesized by anchoring binary lanthanide oxides CeO_2/Nd_2O_3 on GO-wrapped Fe_3O_4 core-shell using a straightforward and economical solvothermal method. The synthesized magnetic photocatalyst was assessed by photo-Fenton degradation of methylene blue in hydrogen peroxide and photoreduction of toxic Cr(VI) in the presence of formic acid under the natural sunlight.

EXPERIMENTAL

All AR-grade chemicals and reagents were purchased from Sigma-Aldrich, USA and utilized without purification.

Synthesis of Fe_3O_4@rGO@CeO_2/Nd_2O_3 magnetic photocatalyst

Synthesis of Fe_3O_4@GO: $FeCl_3 \cdot 6H_2O$ (1 mmol), sodium dodecylbenzene sulfonate (SDBS, 1 mmol) as a surfactant and sodium acetate (1 mmol) was mixed in 70 mL ethylene glycol and sonicated for 30 min. The above mixture was subjected to a Teflon-lined autoclaved reactor and put in an oven at 180 ºC for about 10 h. A blackish-brown product was obtained, separated by an external magnet and washed several times with distilled water and ethanol. The product was dried in a vacuum oven at 60 ºC for 12 h [33-35]. The prepared Fe_3O_4 (0.4 g) was dispersed in 100 mL isopropyl alcohol by ultrasonic for 30 min. Afterward, 1 mL (3-aminopropyl)trimethoxysilane (APTMS) was added dropwise into the above mixture and refluxed for 24 h at 80 ºC to obtain Fe_3O_4@APTMS [36,37]. Finally, 150 mL of graphene oxide (GO) solution synthesized by the modified Hummer's method was mixed with a homogeneous solution of Fe_3O_4@APTMS and vigorously stirred for 1 h to get GO wrapped Fe_3O_4 (Fe_3O_4@GO). SDBS was added as a surfactant to increase the stability and bonding between Fe_3O_4 and reduced graphene oxide [38,39].

Solvothermal synthesis of Fe_3O_4@rGO@CeO_2/Nd_2O_3: The two compositions of Fe_3O_4@rGO@CeO_2/Nd_2O_3 nanocomposite with the molar proportion of Fe_3O_4@rGO with other salts as 1:1:1 and 1:0.5:0.5 have been synthesized as follows: For synthesizing a 1:1:1 ratio for nanocomposite, 1 mmol of Fe_3O_4@GO was effectively dispersed in 50 mL of ethylene glycol by ultrasonic treatment for 30 min. Then, $Ce(NO_3)_3 \cdot 6H_2O$ (1 mmol) and $NdCl_3 \cdot 6H_2O$ (1 mmol) were separately dispersed in a beaker using 20 mL ethylene glycol and ultrasonicated for 30 min. Then, all three solutions were mixed, stirred for 20 min followed by the addition of ammonia solution (3 mmol) was added dropwise to get a purple solution. The mixture was then subjected to a Teflon-lined autoclaved reactor and put in an oven at 200 ºC for about 10 h. The resultant product was subjected to magnetic separation and washed with distilled water and ethanol to remove residual unreacted salt effectively.

Finally, the obtained Fe_3O_4@rGO@CeO_2/Nd_2O_3 was dried in a vacuum oven at 60 ºC for 24 h and then calcinated for 4 h at 550 ºC to get fine powder of magnetic photocatalyst [28-30]. Similarly, for synthesis Fe_3O_4@rGO@CeO_2/Nd_2O_3 (1:0.5:0.5) nanocomposite procedure is same as described above only change in proportion of salt is different (1 mmol Fe_3O_4@GO: 0.5 mmol $Ce(NO_3)_3{\cdot}6H_2O$: 0.5 mmol $NdCl_3{\cdot}6H_2O$). In similar manner, binary lanthanide CeO_2/Nd_2O_3 nanocomposite has been prepared by above procedure without adding Fe_3O_4@GO.

Characterization: The surface morphology and elemental composition of synthesized samples were evaluated using a field emission scanning electron microscope (FESEM) with an attached energy dispersive X-ray spectrometer (EDX) Carl ZEISS supra-55. High-resolution transmission electron microscope (HRTEM) investigation was performed using Joel TEM 2100 plus with an Operating voltage of 20-300 kV and Resolution 2.4 A.U. The X-ray diffraction (XRD) patterns of the photocatalyst were analyzed with a Rigaku X-ray diffractometer using the Cu*K*α radiation (λ = 1.5405 Å) between an angle range of 2θ = 10º-80º. The FTIR studies of the samples were performed with a Perkin-Elmer Spectrum IR Version 10.7.2 FTIR spectrophotometer, The stability of the nanocomposite was analyzed by thermogravimetric analysis (TGA), differential thermal analysis (DTA) and differential scanning calorimetry (DSC) using NETZSCH STA 2500 with temperature ranges varying from 30 ºC to 900 ºC. Magnetic characterization was done by Micro sense EZ-9 vibrating sample magnetometer (VSM) at moderate temperature. The absorption spectra, photoreduction reaction and dye degradation analysis were recorded using a UV-visible spectrophotometer (Shimadzu UV-1800).

Photocatalytic dye degradation: The methylene blue (MB) dye was used as a model dye to check the photocatalytic performance of as-synthesized nanocomposites. In this photocatalytic study, 10 mg of photocatalyst was added in 50 mL of 25 ppm aqueous methylene blue dye solutions, 2 mL H_2O_2 (0.0536 M) was added, stirred in the dark for 30 min to attain equilibrium and then the aqueous dye solutions were continually irradiated under natural sunlight to achieve photo-Fenton degradation. The experiments were conducted under similar conditions on sunny days between 11:00 and 14:00 during October-November 2023 at 30 ºC. The experimental setup used for photodegradation and photoreduction was mentioned earlier [37]. At regular intervals, 4 mL of dye solution was examined with a UV-visible spectrophotometer [33,37,40]. The photocatalytic degradation efficiency of the samples was determined by employing the subsequent mathematical expression [40].

$$\text{Photocatalytic efficiency (\%)} = \frac{C_o - C_t}{C_o} \times 100 \qquad (1)$$

where C_o = initial dye concentration, C_t = concentration of methylene blue dye at various times (t).

Photocatalytic reduction of chromium(VI): The synthesized Fe_3O_4@rGO@CeO_2/Nd_2O_3 nanocomposite was used as a magnetic photocatalyst to reduce Cr(VI). In this typical experiment, 100 ppm $K_2Cr_2O_7$ was prepared as stock. A stock solution (100 mL) was taken in a 250 mL of beaker containing 2 mL formic acid and 10 mg catalyst and stirred for 30 min to achieve equilibrium. Then, the above mixture was continuously irradiated under sunlight. Similar experimental conditions were used as described for dye degradation mentioned above. After each 10 min interval, a 4 mL solution was taken and examined using a UV-visible spectrophotometer. The performance of the photocatalyst was evaluated by analyzing a reduction in the characteristic absorption band of Cr(VI) at 350 nm as a function of irradiation time [3,37,41-43].

RESULTS AND DISCUSSION

XRD studies: A powder X-ray diffraction (XRD) analysis was studied to assess the magnetic photocatalyst's crystallographic arrangement and phase homogeneity. To identify the complete synthesis of prepared Fe_3O_4@rGO@CeO_2/Nd_2O_3 photo-catalyst in two different compositions, it was compared with Fe_3O_4 and CeO_2/Nd_2O_3 binary nanocomposite in Fig. 1. For pure Fe_3O_4, the peaks at 2θ of 18.65º, 30.30º, 35.68º, 43.49º, 57.30º and 62.85º are best matched with the cubic phase structure (JCPDS No. 96-900-5840). Also, the XRD patterns of two compositions of photocatalyst exhibits similar distinct peaks with different intensities at 2θ of 15.67º, 17.58º, 22.37º, 23.70º, 24.99º, 25.20º, 27.36º, 28.60º, 32.95º, 33.91º, 35.59º, 39.06º, 39.93º, 45.54º, 46.45º and 52.74º, are also best matched with the cubic structure of CeO_2/Nd_2O_3 (JCPDS No. 00-028-0266) with empirical formula $Ce_{0.75}Nd_{0.25}O_{1.88}$ [30,44] as shown in Fig. 1.

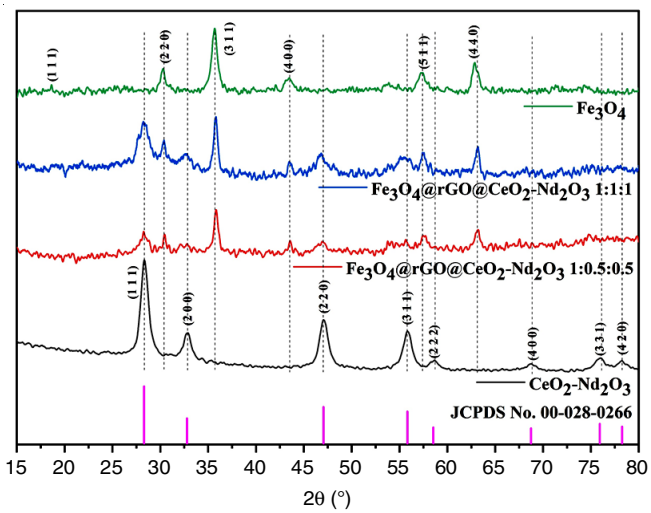

Fig. 1. Comparative X-ray diffraction patterns of Fe_3O_4, CeO_2/Nd_2O_3, Fe_3O_4@rGO@CeO_2/Nd_2O_3 (1:0.5:0.5) and Fe_3O_4@rGO@CeO_2/Nd_2O_3 (1:1:1) nanocomposite with JCPDS file of CeO_2/Nd_2O_3

The XRD pattern of two compositions of Fe_3O_4@rGO@CeO_2/Nd_2O_3 shows reflection (1 1 1), (2 2 0), (2 0 0), (3 1 1), (4 0 0), (2 2 0), (3 1 1), (5 1 1), (2 2 2), (4 4 0), (4 0 0), (3 3 1) and (4 2 0), which clearly indicates presence of Fe_3O_4 and CeO_2/Nd_2O_3 in a nanocomposite and all belonging to a cubic crystalline structure. The crystallite size of Fe_3O_4, CeO_2/Nd_2O_3, Fe_3O_4@rGO@CeO_2/Nd_2O_3 (1:0.5:0.5) and Fe_3O_4@rGO@ CeO_2/Nd_2O_3 (1:1:1) was determined using the full width at half maximum (FWHM) of the most prominent peak by using Debye-Scherrer's equation [45,46]. The average crystallite size observed from

the XRD pattern for Fe_3O_4, CeO_2-Nd_2O_3, Fe_3O_4@rGO@CeO_2/Nd_2O_3 (1:0.5:0.5) and Fe_3O_4@rGO@CeO_2/Nd_2O_3 (1:1:1) nanocomposite are 8 nm, 10 nm, 12 nm and 16 nm, respectively.

FESEM studies: The morphology and microstructure of pure Fe_3O_4, Fe_3O_4@rGO@CeO_2/Nd_2O_3 (1:0.5:0.5) and Fe_3O_4@rGO@CeO_2/Nd_2O_3 (1:1:1) were analyzed using FE-SEM micrographs. Fig. 2 (a, a_1), (b, b_1) and (c, c_1) shows the detailed scanning electron micrographs of Fe_3O_4 nanoparticles, Fe_3O_4@rGO@CeO_2/Nd_2O_3 (1:0.5:0.5) and Fe_3O_4@rGO@CeO_2/Nd_2O_3 (1:1:1), respectively at different magnifications. Images of Fe_3O_4 showed that the material consisted of nanosized particles smaller than 100 nm, with spherically shaped grains that clung together in very dense aggregates of Fe_3O_4 nanoparticles. This clustering of nanoparticles results in greater magnetostatic coupling between nanoparticles. The average particle size observed by Fe_3O_4 nanoparticles is around 52.16 nm, as shown in the histogram. As the deposition of CeO_2/Nd_2O_3 takes place on Fe_3O_4@rGO during the formation of magnetic photocatalyst, the average particle size increases up to 55.30 nm for Fe_3O_4@rGO@CeO_2/Nd_2O_3 (1:0.5:0.5). As the concentration of CeO_2 and Nd_2O_3 increases, the average particle size increases to 63.06 nm. The particles are spherically shaped with less aggregation as compared to Fe_3O_4

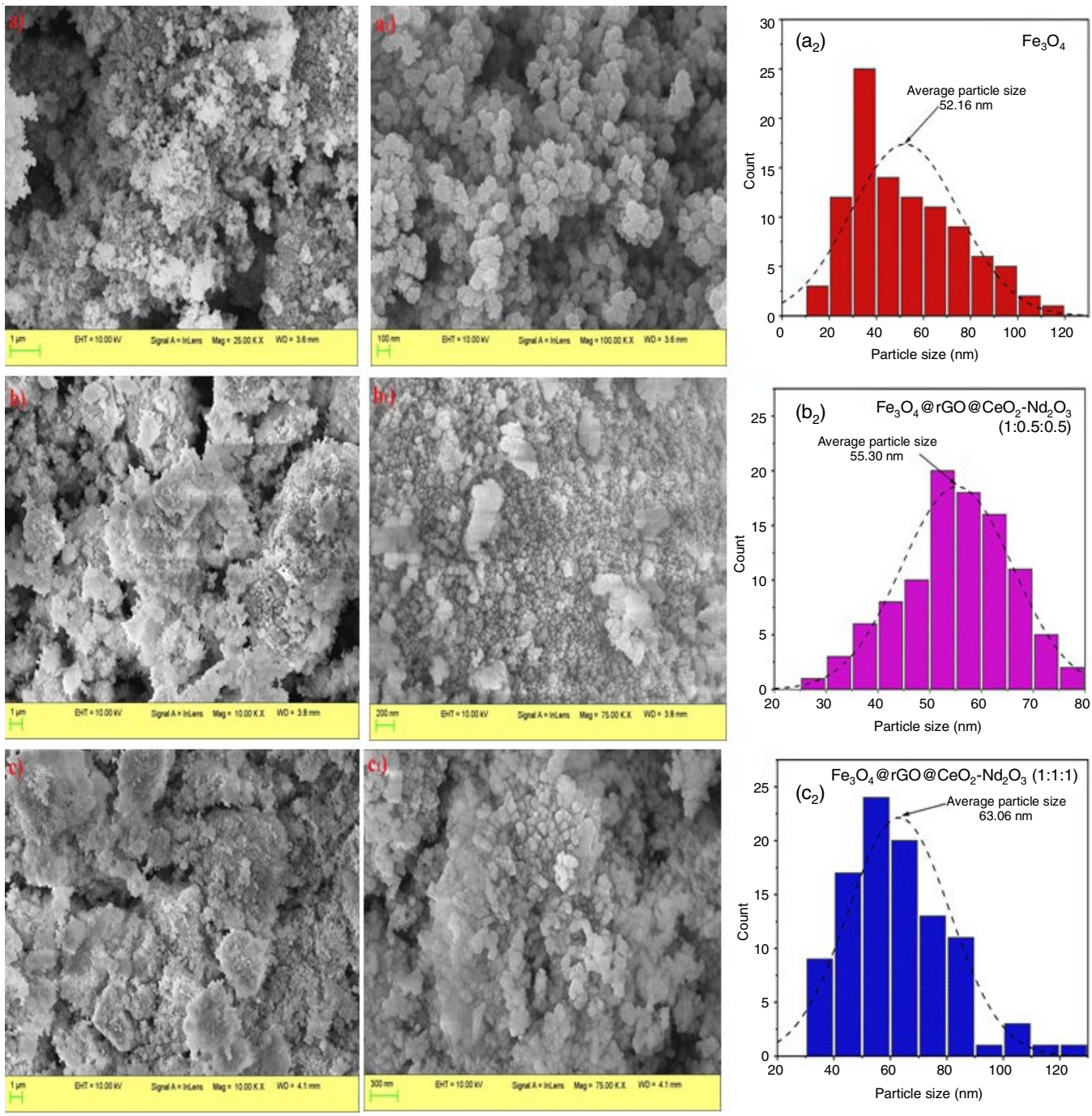

Fig. 2. FE-SEM images of (a, a_1) Fe_3O_4, (b, b_1) Fe_3O_4@rGO@CeO_2/Nd_2O_3(1:0.5:0.5), (c,c_1) Fe_3O_4@rGO@CeO_2/Nd_2O_3(1:1:1) and Histogram of (a_2) Fe_3O_4, (b_2) Fe_3O_4@rGO@CeO_2/Nd_2O_3(1:0.5:0.5), (c_2) Fe_3O_4@rGO@CeO_2/Nd_2O_3(1:1:1)

nanoparticles, as shown in Fig. 2 (b, b_1) and (c, c_1), which indicates the formation of Fe_3O_4@rGO@CeO_2/Nd_2O_3 nanocomposite with decreased magnetic properties.

EDX studies: The elemental composition of Fe_3O_4@rGO @CeO_2/Nd_2O_3 was analyzed with the help of an energy-dispersive X-ray (EDX) spectrometer linked with SEM. Fig. 3(a-b) depicts the EDX spectra of Fe_3O_4 and Fe_3O_4@rGO@CeO_2/Nd_2O_3 (1:1:1) nanocomposite. A pure sample of Fe_3O_4 shows EDX data of weight% as Fe (39.68%) and O (60.32%) (Fig. 3a). In contrast, the Fe_3O_4@rGO@CeO_2/Nd_2O_3(1:1:1) nanocomposite shows EDX data as Fe (32.48%), Ce (19.58%), Nd (13.24%), O (24.53%), C (9.13%) and Si (1.03%) (Fig. 3b). The obtained EDX spectra provide evidence of the existence of iron (Fe), cerium (Ce), neodymium (Nd), oxygen (O), carbon (C) and silicon (Si) within the Fe_3O_4@rGO@CeO_2/Nd_2O_3 composites. Significantly, no additional elements are detected, suggesting that the synthesized photocatalyst possesses a high purity level devoid of impurities.

TEM and SAED studies: Fig. 4(a-i) shows the TEM images of Fe_3O_4, CeO_2/Nd_2O_3 and Fe_3O_4@rGO@CeO_2/Nd_2O_3, d-spacing and selected area diffraction (SAED) pattern of Fe_3O_4 and Fe_3O_4 @rGO@CeO_2/Nd_2O_3. The HRTEM image of CeO_2/Nd_2O_3 clearly shows that CeO_2 nanoparticles have crystalline nanorods structure with an average length of 90 nm and diameter of 42 nm on which Nd_2O_3 nanoparticles are deposited [47-49]. The HRTEM image inset with interplanar distance for CeO_2 nanorods is shown in Fig. 4(f) with a d-spacing 0.312 nm of (1 1 1) plane. The complete synthesis of Fe_3O_4@rGO wrapped CeO_2/Nd_2O_3 is clearly observed in TEM images [Fig. 4(g,h)]. From TEM images, it can clearly be seen that Fe_3O_4 nanoparticles are completely wrapped on rGO sheets and CeO_2/Nd_2O_3 is deposited on the reduced graphene oxide sheets. The SAED pattern reveals that Fe_3O_4@rGO@CeO_2/Nd_2O_3 is polycrystalline in nature. The SAED pattern reveals a single crystalline nature of CeO_2 nanorods, however, the emergence of bright spots signifies the formation of polycrystalline photocatalysts.

FTIR studies: The FTIR spectra of Fe_3O_4, Fe_3O_4@rGO, CeO_2/Nd_2O_3, Fe_3O_4@rGO@CeO_2/Nd_2O_3 nanocomposite was observed in the range 4000-400 cm^{-1} as shown in Fig. 5. The FTIR spectra of Fe_3O_4, Fe_3O_4@rGO and Fe_3O_4@rGO@CeO_2/Nd_2O_3 show a distinct absorption band around 640-561 cm^{-1}, which corresponds to the spinel cubic structure and is labeled as Fe-O and not seen in CeO_2/Nd_2O_3 clearly indicates the presence of Fe_3O_4 in nanocomposite [50,51]. The absorption band at 3420 cm^{-1} was due to the stretching vibration of a hydroxyl group (-OH), indicating the presence of water in the sample, which is not observed in the IR spectra of CeO_2/Nd_2O_3 shows that nanocomposite is free from moisture. In addition, the absorption band around 1618-1593 cm^{-1} should be symmetric stretching vibrations of the surface hydroxyl groups. In Fe_3O_4@rGO@CeO_2/Nd_2O_3 nanocomposite, the absorption band at 3437 cm^{-1} is due to the presence of acidic -OH groups, which

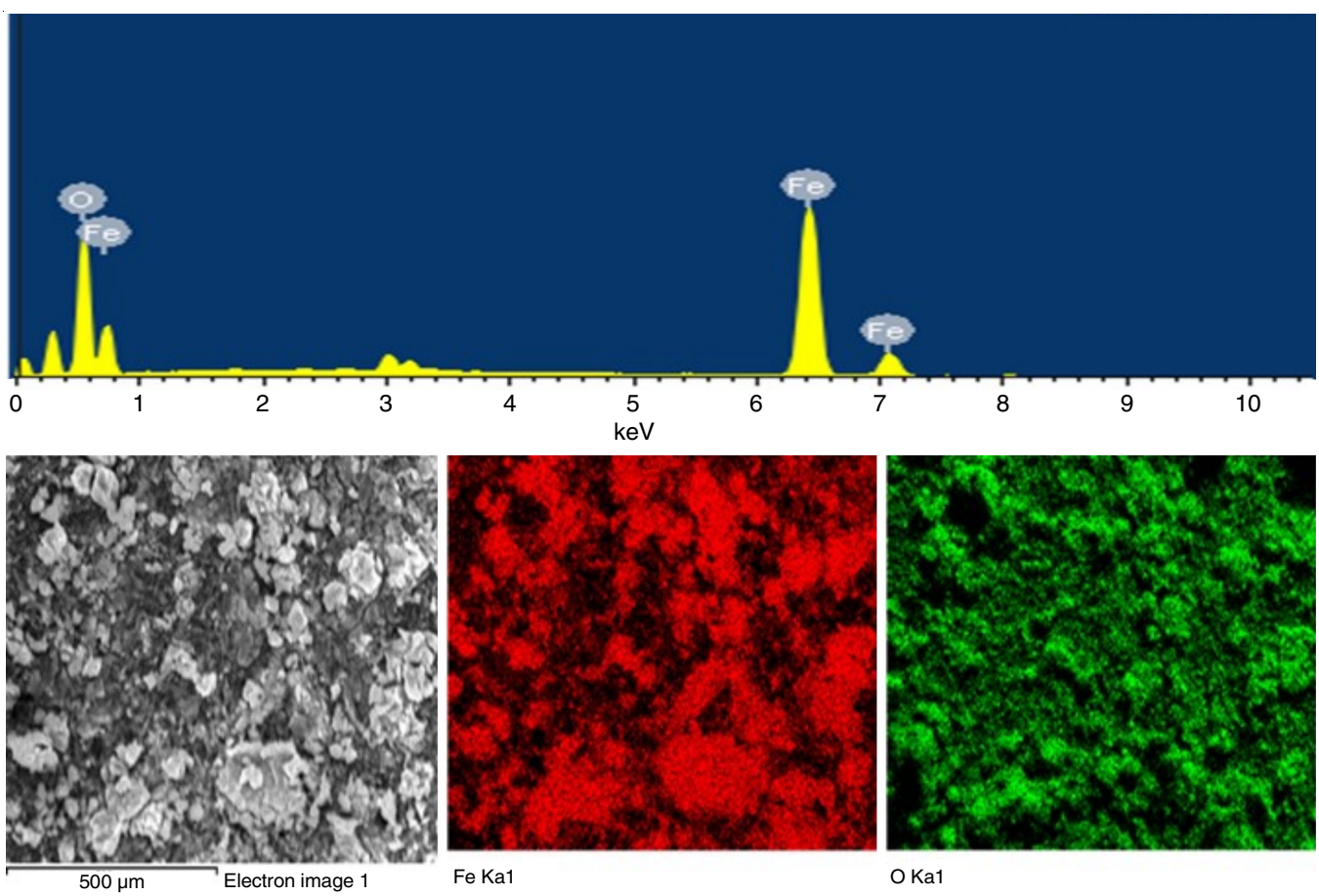

Fig. 3a. EDX Spectra with elemental mapping of Fe_3O_4 nanoparticles

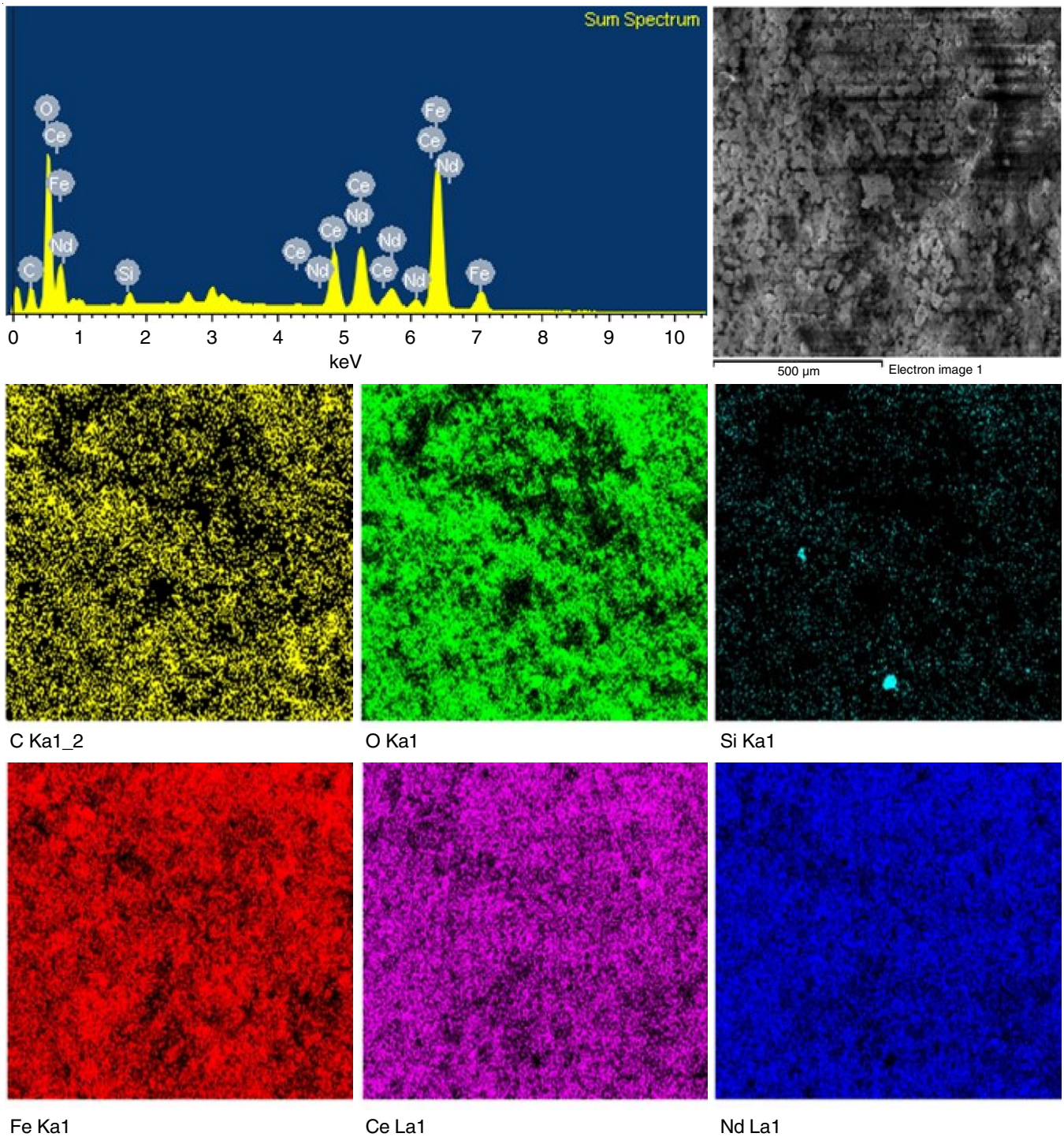

Fig. 3b. EDX Spectra with elemental mapping of Fe_3O_4@rGO@CeO_2/Nd_2O_3 (1:1:1) nanocomposite

confirms that rGO is well wrapped in nanocomposite. Nd_2O_3 nanoparticles are observed in FTIR spectra at an absorption band of 669 cm^{-1} due to Nd-O stretching vibration and Ce-O vibrational stretching followed at absorption band 852 cm^{-1} confirms that CeO_2/Nd_2O_3 is well deposited on the surface of Fe_3O_4@rGO [15,26,30].

UV-visible studies: The UV-visible absorption spectra of the synthesized Fe_3O_4, Fe_3O_4@rGO, CeO_2/Nd_2O_3, Fe_3O_4@rGO@CeO_2/Nd_2O_3 nanocomposite are shown in Fig. 6a. The Tauc plot of $(\alpha h\nu)^{1/2}$ against the photon energy (eV) was plotted to determine the indirect bandgap represented in Fig. 6b. The spectra show the broad absorption in the UV-visible region for the Fe_3O_4@rGO@CeO_2/Nd_2O_3 in the range 250-400 nm. The Fe_3O_4@rGO@CeO_2/Nd_2O_3 nanocomposite has strong absorption peaks at 330 nm with a discernible redshift. The observed redshift can potentially be attributed to the composition of Fe_3O_4-wrapped rGO sheets and CeO_2/Nd_2O_3 [52]. These strong absorption peaks reveal that Fe_3O_4@rGO@CeO_2/Nd_2O_3 nanocomposite is a good candidate for photocatalytic applications. The Tauc plot exhibits two discernible transitions

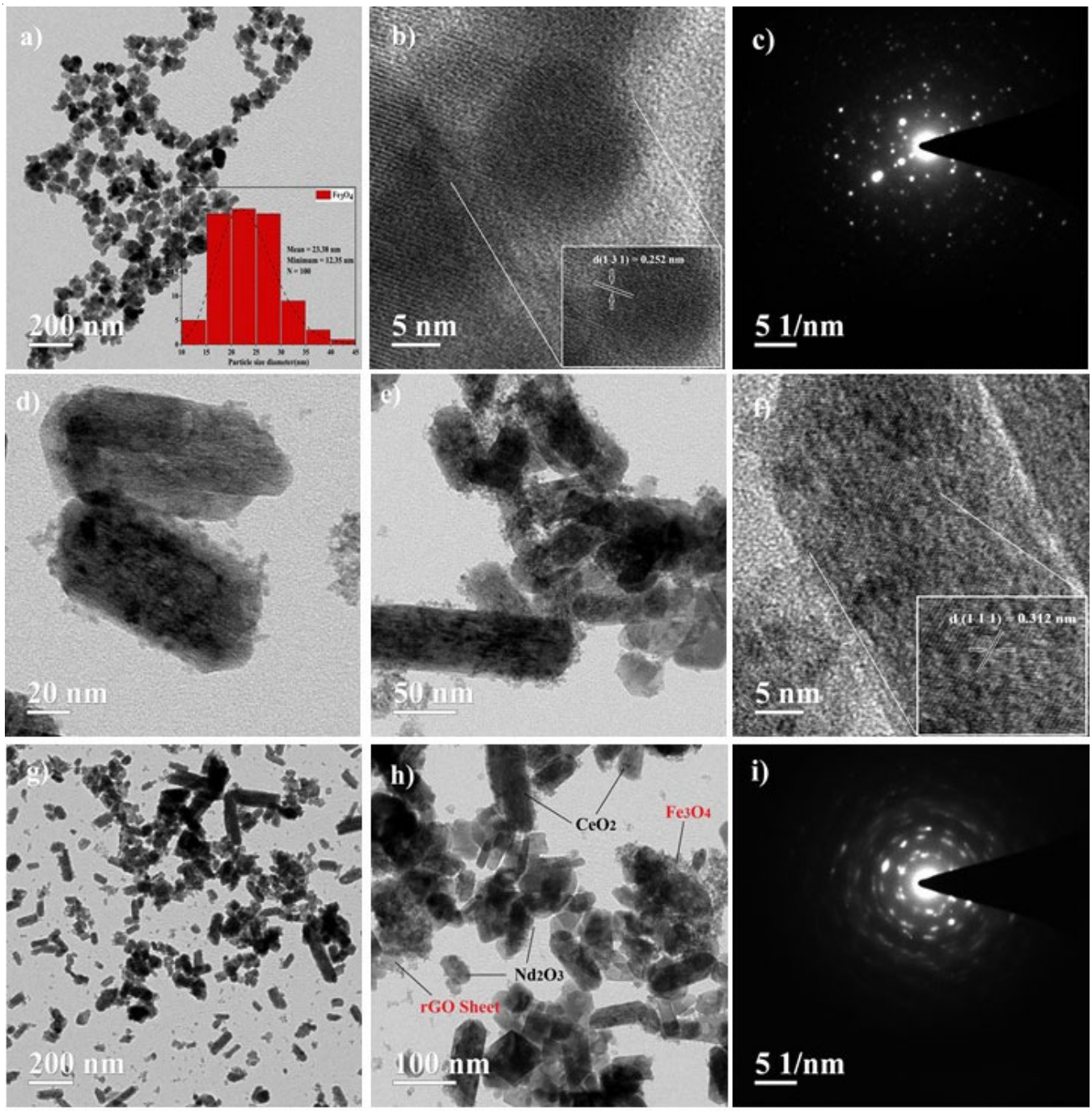

Fig. 4. TEM images of (a) Fe_3O_4 (inset: Histogram) (d,e) CeO_2/Nd_2O_3 and (g, h) Fe_3O_4@rGO@CeO_2/Nd_2O_3 (1:1:1), HRTEM images (inset: d-spacing of (b) Fe_3O_4, (f) CeO_2 nanoparticles), SAED patterns of (c) Fe_3O_4, (i) Fe_3O_4@rGO@ CeO_2/Nd_2O_3 (1:1:1)

as illustrated in Fig. 6b. The initial transition, symbolized by the coloured solid line, is the optical gap that arises from forming an exciton or electron-hole pair, referred to as a Frenkel exciton. The fundamental energy differential between the valence band (VB) and conduction band (CB) is symbolized by coloured dashed lines during the second transition [37,53]. The Tauc plot reveals the following values for the indirect band gaps (optical energy gap) of various nanocomposites: Fe_3O_4 at 2.90 eV, CeO_2/Nd_2O_3 at 2.27 eV, Fe_3O_4@rGO at 2.19 eV and Fe_3O_4 @rGO@CeO_2/Nd_2O_3 at 2.14 eV. Additionally, the indirect band gaps (fundamental energy gap) for Fe_3O_4, Fe_3O_4@rGO, CeO_2/Nd_2O_3, Fe_3O_4@rGO@CeO_2/Nd_2O_3 were observed at 3.85 eV, 3.91 eV, 3.1 eV and 3.68 eV, respectively.

Magnetic measurements (VSM): The room temperature magnetization measurements of Fe_3O_4, Fe_3O_4@rGO@CeO_2/Nd_2O_3 (1:0.5:0.5) and Fe_3O_4@rGO@CeO_2/Nd_2O_3 (1:1:1) nanocomposites were performed by using a vibrating sample magnetometer (VSM). As shown in Fig. 7, the saturation magnetization (MS) of Fe_3O_4 determined was 101.84 emu/g, which signifies a notable magnetization power attributed to the aggregation of nanoparticles. While the saturation magnetization (MS) of Fe_3O_4@rGO@CeO_2/Nd_2O_3 (1:0.5:0.5) and (1:1:1) were meas-

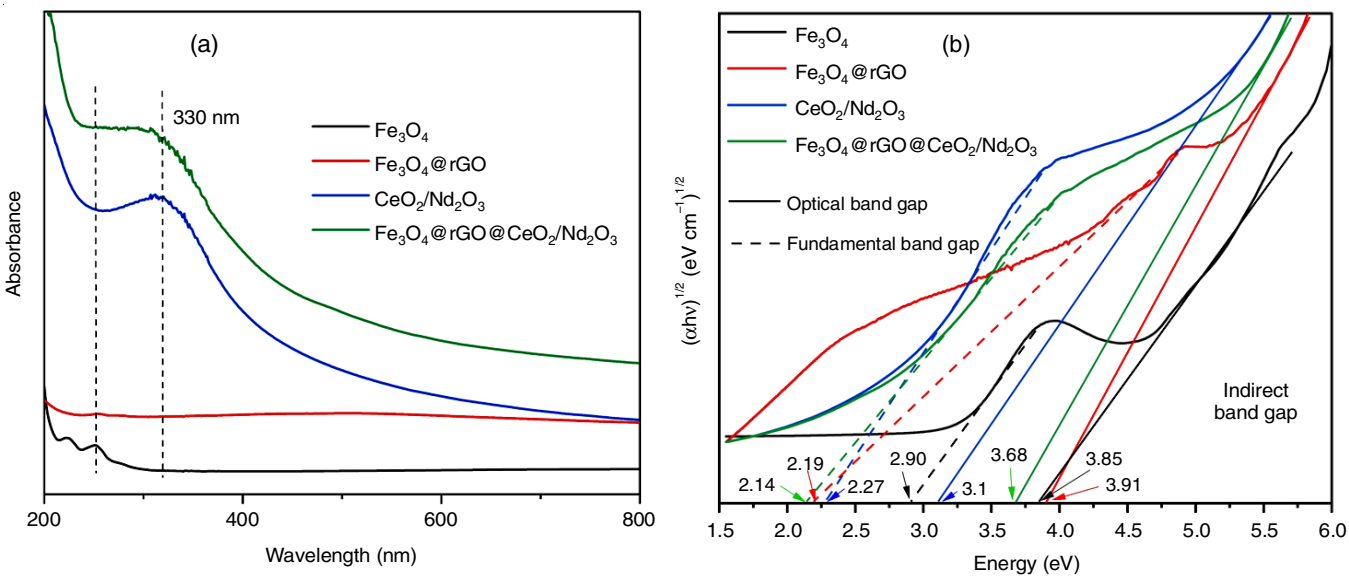

Fig. 6. (a) UV-visible spectra, (b) Tauc plot (indirect band gap) of Fe_3O_4, Fe_3O_4@rGO, CeO_2/Nd_2O_3, Fe_3O_4@rGO@CeO_2/Nd_2O_3 nanocomposites

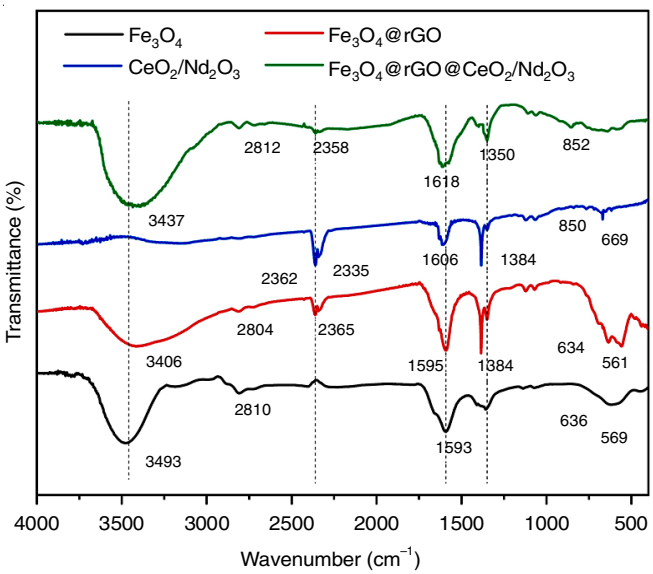

Fig. 5. FTIR spectra of Fe_3O_4, Fe_3O_4@rGO, CeO_2/Nd_2O_3, Fe_3O_4@rGO@CeO_2/Nd_2O_3 nanocomposite

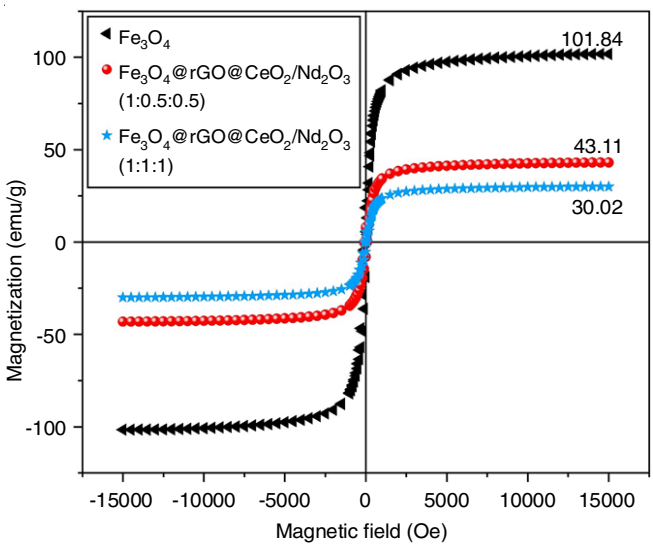

Fig. 7. VSM analysis of Fe_3O_4, Fe_3O_4@rGO@CeO_2/Nd_2O_3 (1:0.5:0.5) and Fe_3O_4@rGO@CeO_2/Nd_2O_3 (1:1:1)

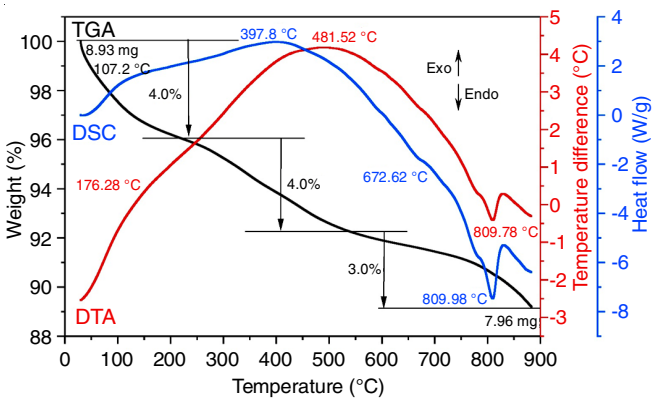

Fig. 8. TGA, DSC and DTA curve of Fe_3O_4@rGO@CeO_2/Nd_2O_3 (1:1:1)

ured to be 43.11 emu/g and 30.02 emu/g, respectively. This relatively low value can be attributed to rGO wrapped on the Fe_3O_4 surface and the subsequent anchoring of CeO_2 and Nd_2O_3 nanoparticles with different proportions. An external magnetic field separates nanocomposite photocatalyst from solution for reuse.

Thermal analysis: TGA, DTA and DSC curve analysis are primarily employed to examine the thermal stability, degradation, moisture content and chemical changes of the nanomaterials. The TGA, DTA and DSC curves of Fe_3O_4@rGO@CeO_2/Nd_2O_3 nanocomposites are shown in Fig. 8 with temperature range from 10 to 900 ºC. The TGA curve showed that the synthesized nanocomposite was decomposed in three steps with total weight losses of around 11.0%. In TGA curve, first, 4.0% weight loss occurs at 220 ºC due to the loss of water molecules in the synthesized nanocomposite. A consecutive weight loss of 4.0% in the temperature range of 220 ºC to 550 ºC was due to oxidation of Fe_3O_4 to Fe_2O_3 and the decomposition of reduced graphene oxide occurs simultaneously [54]. At the end of the heating, a 3% weight loss is observed from 550 ºC to 880 ºC,

which is attributed to the phase transfer, decomposition or degradation of nanocomposite material. The overall loss of 11.0% up to 880 ºC in TGA indicated the high thermal stability of Fe_3O_4@ rGO@CeO_2/Nd_2O_3 nanocomposite.

The DSC curve of synthesized nanocomposite exhibits three exothermic peaks at 107.2 ºC, 397.8 ºC and 672.62 ºC and one sharp endothermic peak at 809.98 ºC. The peak of 107.2 ºC in the DSC curve shows the removal of the adsorbed water from the nanocomposite. The peak at 397.8 ºC clearly indicates the oxidation and complete transformation of Fe_3O_4 to Fe_2O_3 [55]. The third exothermic peak at 672.62 ºC in the DSC curve relates to the decomposition of lanthanide oxide nanocomposites. Also, the DSC curve showed an intense endothermic peak at 809.98 ºC, which relates to the phase transfer of the synthesized nanocomposite.

For the DTA curve of Fe_3O_4@rGO@CeO_2/Nd_2O_3 nanocomposite, a strong exothermic peak at 481.52 ºC was observed which contributed to the complete oxidation of Fe_3O_4 to Fe_2O_3 and the decomposition of reduced graphene oxide was also confirmed by TGA and DSC curves. Similarly, like DSC, a peak at about 809.78 ºC is also observed in DTA, which favours the phase transfer, decomposition and degradation of the synthesized nanocomposite.

Applications

Photo-fenton degradation of methylene blue dye, active species trapping experiment and possible mechanism: Methylene blue dye was selected as a model dye to analyze the degradation activity of synthesized Fe_3O_4@rGO@CeO_2/Nd_2O_3 (1:1:1) magnetic nanocomposite and compare it with Fe_3O_4, CeO_2/Nd_2O_3 and Fe_3O_4@ CeO_2/Nd_2O_3 nanocomposite in presence and absence of H_2O_2. The decrease in the concentration of methylene blue dye was examined by determining the absorbance at a 662 nm wavelength. A 25 ppm methylene blue dye solution with 10 mg of photocatalyst was stirred for 30 min in dark to achieve adsorption-desorption equilibrium. The photo-Fenton reaction was initiated by the introducing 2 mL of H_2O_2 (0.0536 M) to the system and putting the whole mixture under sunlight at 30 ºC without any external light source, resulting in the conversion of ferric (Fe^{3+}) to ferrous (Fe^{2+}), which accelerated the degradation process [33,56].

The progress of photocatalytic methylene blue dye degradation by Fe_3O_4@rGO@CeO_2/Nd_2O_3 is shown in Fig. 9. When the solution was agitated in the absence of light to achieve adsorption-desorption equilibrium, no significant adsorption by photocatalysts was found for the methylene blue dye. The degradation efficiency of Fe_3O_4@rGO@CeO_2/Nd_2O_3 magnetic photocatalyst was 98% in 50 min. At neutral pH, the photocatalytic degradation of 25 ppm methylene blue with various photocatalysts and H_2O_2 doses is shown in Fig. 10a.

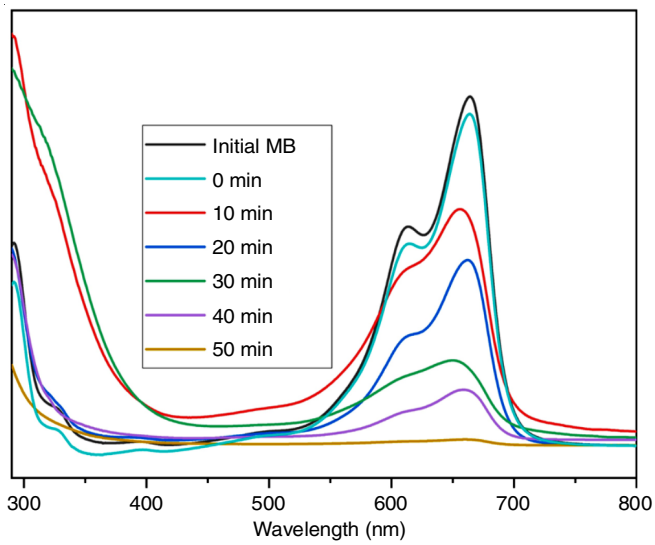

Fig. 9. UV spectra absorption of methylene blue dye degradation by Fe_3O_4@rGO@CeO_2/Nd_2O_3 at neutral pH and 0.0536 M H_2O_2 dose

Several scavengers were used to identify the active species involved in the photo-Fenton reaction. $AgNO_3$, EDTA, isopropyl alcohol and *p*-benzoquinone were utilized as scavengers

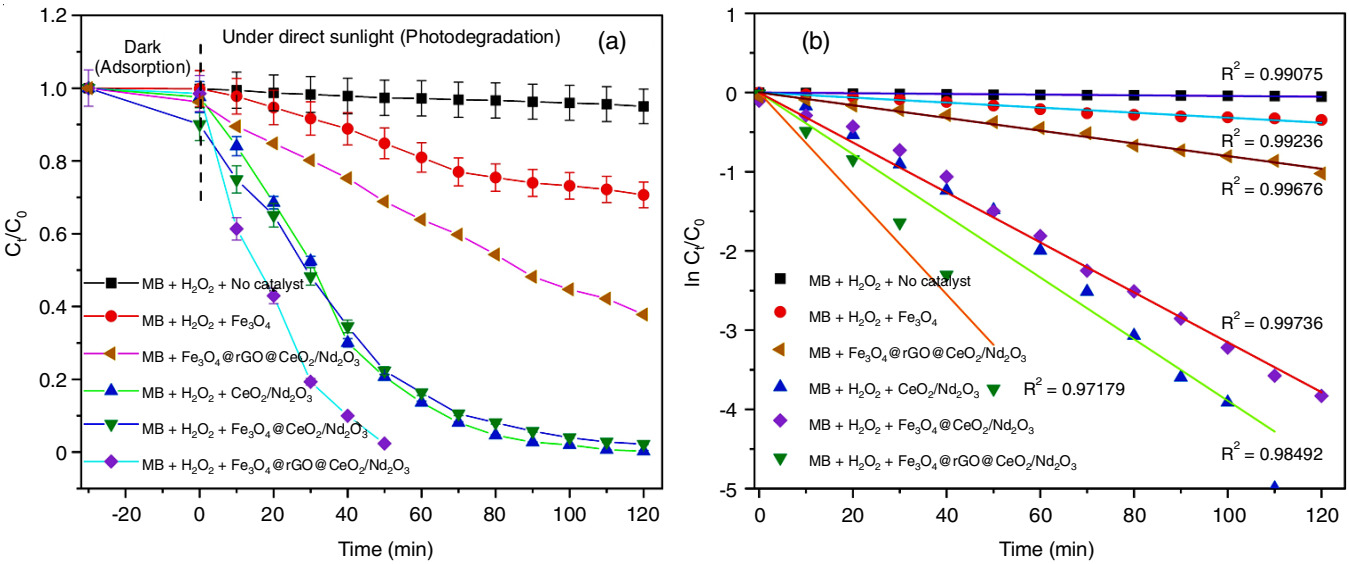

Fig. 10. (a) Photo-Fenton degradation of methylene blue at neutral pH by different photocatalysts and (b) Kinetic study plot of ln (C_t/C_0) *versus* time

for active species such as electrons (e^-), holes (h^+), hydroxyl radicals ($OH^•$) and superoxide radicals (O_2^-) [37,57]. The photodegradation efficiency decrease to 14%, 21% and 26% when IPA, EDTA and $AgNO_3$ (1 mmol) were added to the dye solution. Fig. 11 illustrates that the photo-Fenton reaction is driven by hydroxyl radicals ($OH^•$), holes (h^+), followed by electrons (e^-). *p*-Benzoquinone (BQ) has limited influence on the photodegradation, retaining around 95%, confirming the low role of superoxide radicals ($O_2^{•-}$) in the photo-Fenton process. Based on the trapping experiment, the hydroxyl radicals ($OH^•$) significantly contributes to photodegradation of H_2O_2.

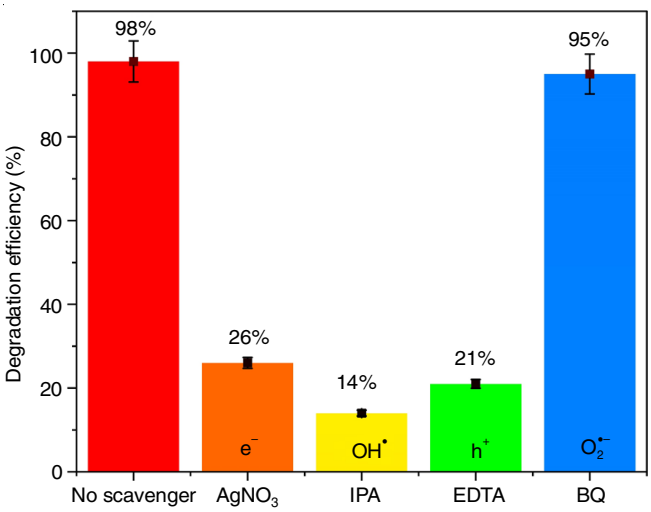

Fig. 11. Effect of various scavengers on the photo-Fenton degradation of methylene blue dye by Fe_3O_4@rGO@CeO_2/Nd_2O_3

It is also clear from Fig. 10(a-b) that H_2O_2 doses in the Fenton system increase the photocatalytic degradation activity by generating hydroxyl radicals ($OH^•$). Also, the addition of CeO_2 and Nd_2O_3 on the surface of graphene oxide traps electrons, which controls the electron-hole recombination for the effective degradation of methylene blue dye. Improved photo-Fenton activity is shown by synthesized Fe_3O_4@rGO@CeO_2/Nd_2O_3 nanocomposite due to a small band gap of 2.14 eV. Graphene oxide plays a significant role by suppressing the recombination of photogenerated electron-hole pairs produced by Fe_3O_4, CeO_2 and Nd_2O_3, enhancing the photocatalytic activity [58]. The possible mechanism of the photo-Fenton methylene blue dye degradation process can be briefly described in the following equations [33,59,60]:

$$Fe^{2+} + H_2O_2 \longrightarrow Fe^{3+} + OH^- + OH^• \quad (2)$$

$$Fe_3O_4 + h\nu \longrightarrow Fe_3O_4\,(e^- + h^+) \quad (3)$$

$$Fe_3O_4\,(h^+) + OH^- \longrightarrow OH^• \quad (4)$$

$$Fe_3O_4\,(h^+) + H_2O \longrightarrow OH^• + H^+ \quad (5)$$

$$CeO_2 \text{ or } Nd_2O_3 + h\nu \longrightarrow CeO_2 \text{ or } Nd_2O_3\,(e^- + h^+) \quad (6)$$

$$Fe^{3+} + CeO_2 \text{ or } Nd_2O_3\,(e^-) \longrightarrow Fe^{2+} \quad (7)$$

$$\text{Methylene blue dye} + OH^•/h^+/e^- \longrightarrow \text{Degradation products } (CO_2 + H_2O) \quad (8)$$

Reaction kinetic studies: The photocatalytic degradation of methylene blue dye by Fe_3O_4@rGO@CeO_2/Nd_2O_3 nanocomposite follows the pseudo-first-order kinetic model as shown in Fig. 10b, which could be expressed as follows [61,62]:

$$\ln\frac{C_t}{C_o} = -k_{abs}(t) \quad (9)$$

where $-k_{abs}$ = pseudo first order rate constant of dye removal [63]. It was observed that Fe_3O_4@rGO@CeO_2/Nd_2O_3 nanocomposite possesses a higher rate constant than CeO_2/Nd_2O_3 and Fe_3O_4 nanoparticles, which is about 0.09204 min^{-1}.

Photocatalytic reduction of chromium(VI) with possible mechanism: Magnetic Fe_3O_4@rGO@CeO_2/Nd_2O_3 nanocomposite was employed for conducting the photocatalytic reduction of Cr(VI) in the presence and absence of formic acid under the influence of natural sunlight. Formic acid was utilized in Cr(VI) photoreduction because it is less toxic and stable; it also provides an acidic medium which is permissive to the reduction of Cr(VI) [7,42,64]. The effect of magnetic nanocomposite and sunlight on photocatalysis at different time laps is shown in Fig. 12a. The adsorption-desorption equilibrium was attained by placing it in dark for 30 min. There is negligible adsorption of Cr(VI) by different photocatalyst on the surface was observed. Afterward, the Cr(VI) solution was kept under natural sunlight and after every 10 min, a photo-reduced solution was collected to check the decrease in adsorption using a UV-visible spectrophotometer. In Fig. 12a, it is clearly observed that almost complete photoreduction of 100 ppm Cr(VI) had been achieved by

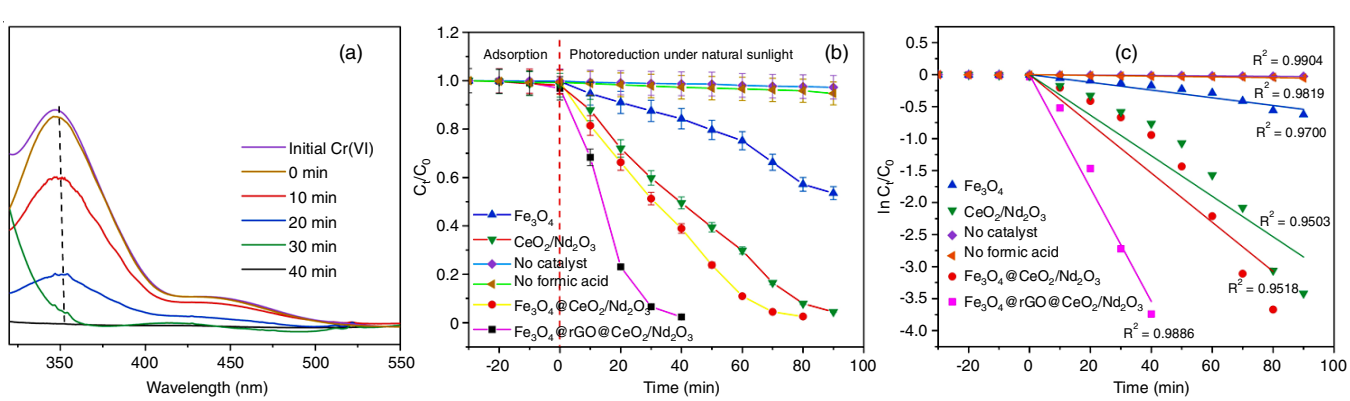

Fig. 12. (a) Photocatalytic chromium(VI) reduction by Fe_3O_4@rGO@CeO_2/Nd_2O_3 in formic acid, (b) photoreduction study of different catalysts, (c) kinetic study plot of photoreduction by a different catalyst

observing a decrease in the absorption band at 350 nm in 40 min. Fig. 12a shows that in the first 10 min, the reduction is about 34%, which increases to 85% in just 30 min and after 40 min, complete photoreduction of Cr(VI) of about 99% observed with rate constant of the reaction is 0.09226 min^{-1}. The photocatalytic study and rate constant of the photoreduction by different catalysts are shown in Fig. 12b-c. The possible mechanism for the photoreduction of hexavalent chromium is described by eqns. 10-17 [64,65]:

$$Fe_3O_4 \text{ or } CeO_2 \text{ or } Nd_2O_3 + h\nu \longrightarrow Fe_3O_4 \text{ or } CeO_2 \text{ or } Nd_2O_3\,(h^+_{VB} + e^-_{CB}) \quad (10)$$

$$HCOOH \longrightarrow CO_2 + H_2 \quad (11)$$

$$H_2O + h^+_{VB} \longrightarrow OH^\bullet + H^+ \quad (12)$$

$$Cr_2O_7^{2-}(Cr^{6+}) + 8H^+ + 3H_2 \longrightarrow 2Cr^{3+} + 7H_2O \quad (13)$$

$$Cr_2O_7^{2-}(Cr^{6+}) + 6e^-_{CB} + 14H^+ \longrightarrow 2Cr^{3+} + 7H_2O \quad (14)$$

$$HCOOH + OH^\bullet \longrightarrow CO_2^{\bullet-} + H_3O^+ \quad (15)$$

$$2HCOO^- + h^+_{VB} \longrightarrow CO_2^{\bullet-} + CO_2 + H_2 \quad (16)$$

$$Cr_2O_7^{2-}(Cr^{6+}) + 2CO_2^{\bullet-} + 10H^+ \longrightarrow 2Cr^{3+} + 2CO_2 + 5H_2O \quad (17)$$

The multifunctional nature of formic acid facilitates the separation of holes and electrons, which is advantageous for the photocatalytic activity of nanocomposite. Consequently, reactive radicals ($CO_2^{\bullet-}$) are produced, thereby enhancing the photocatalytic reduction of Cr(VI) in the presence of Fe_3O_4@rGO@CeO_2/Nd_2O_3 nanocomposite. Formic acid also reacts with hydroxyl radicals ($OH^\bullet$) which produce reactive radicals ($CO_2^{\bullet-}$).

Cyclic photocatalytic study (recyclability test): The synthesized Fe_3O_4@rGO@CeO_2/Nd_2O_3 photocatalyst is very stable, as described by TGA-DTA-DSC analysis up to 880 ºC temperature shown in Fig. 8b. Thus, the catalyst can easily separate from the methylene blue and Cr(VI) solutions by the external magnetic field and for reuse. As shown in Fig. 13, After six recycles, the catalytic activity of Fe_3O_4@rGO@CeO_2/Nd_2O_3 slightly decreased from 98% to 92% and 99% to 94%

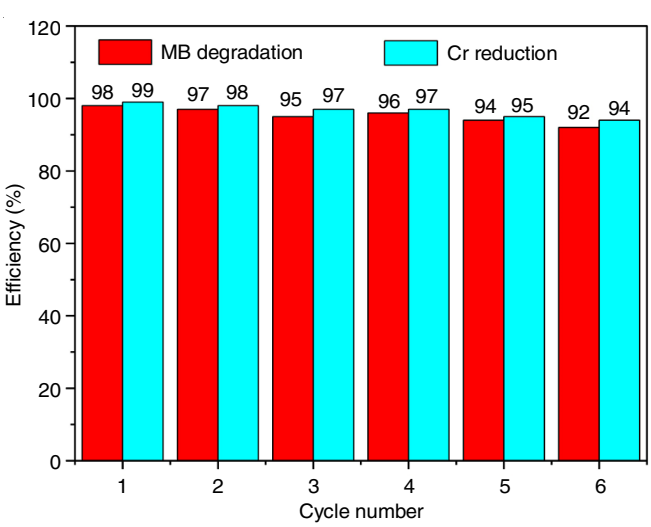

Fig. 13. Cyclic photocatalytic study of Fe_3O_4@rGO@CeO_2/Nd_2O_3 nanocomposite for degradation of methylene blue (MB) and photoreduction of chromium(VI)

for methylene blue degradation and chromium(VI) reduction, respectively. The catalyst has been used multiple times despite its reduced degrading efficiency, suggesting its stability.

Conclusion

In this work, Fe_3O_4@rGO@CeO_2/Nd_2O_3 nanocomposite was synthesized by a simple, efficient and one-step solvothermal method and successfully used for methylene blue dye degradation by photo-Fenton method and Cr(VI) reduction in formic acid when exposed to sunlight. The structural analysis confirmed the cubic spinel spherical structure of Fe_3O_4 and the nanorod structure of CeO_2 on which spherical Nd_2O_3 nanoparticles are deposited. The FESEM and HRTEM images revealed the presence of CeO_2/Nd_2O_3 nanoparticles immobilized on a reduced graphene oxide (rGO) substrate, further encapsulated by spherical Fe_3O_4 nanoparticles. The physico-chemical characteristics of Fe_3O_4@rGO@CeO_2/Nd_2O_3 nanocomposite in the degradation of methylene blue and reduction of Cr(VI) have been studied. Due to the remarkable saturation magnetization exhibited by the photocatalyst, it can effectively extract and undergo recycling processes within the liquid system. The photocatalytic test of the synthesized magnetic photocatalyst for methylene blue degradation and Cr(VI) reduction showed more significant catalytic activity under natural sunlight. A 98% methylene blue degradation is obtained for 2 mL H_2O_2 and 10 mg of magnetic photocatalyst at neutral pH within 50 min. In just 40 min, 99% of the Cr(VI) gets reduced using the same photocatalyst. After six cycles, the photocatalytic activity exhibited slightly decreased catalytic efficiency. In conclusion, the Fe_3O_4@rGO@CeO_2/Nd_2O_3 catalyst exhibits remarkable stability and holds significant promise in the degradation of methylene blue dye and reduction of Cr(VI).

ACKNOWLEDGEMENTS

The authors acknowledge the Department of Chemistry, Karmaveer Bhaurao Patil College (Autonomous), Navi Mumbai and Department of Chemistry Mahatma Phule Arts, Science and Commerce College, Panvel, for providing facilities and technical support. The authors also gratefully acknowledge to the instrumental research facilities provided by Sprint Testing Solutions, Powai, Mumbai, India.

CONFLICT OF INTEREST

The authors declare that there is no conflict of interests regarding the publication of this article.

REFERENCES

1. S.F. Tadesse, D.H. Kuo, W.L. Kebede and G.S. Wolde, *Appl. Surf. Sci.*, **569**, 151091 (2021); https://doi.org/10.1016/j.apsusc.2021.151091
2. F.C. Richard and A.C.M. Bourg, *Water Res.*, **25**, 807 (1991); https://doi.org/10.1016/0043-1354(91)90160-R
3. E. Kalantari, M.A. Khalilzadeh and D. Zareyee, *J. Inorg. Organomet. Polym. Mater.*, **31**, 319 (2021); https://doi.org/10.1007/s10904-020-01784-3
4. A. Zhitkovich, *Chem. Res. Toxicol.*, **24**, 1617 (2011); https://doi.org/10.1021/tx200251t
5. V.K. Gupta, D. Mohan, S. Sharma and K.T. Park, *Environmentalist*, **19**, 129 (1998); https://doi.org/10.1023/A:1006693017711

6. R.W. Herschy, in eds.: L. Bengtsson, R.W. Herschy and R.W. Fairbridge, Water Quality for Drinking: WHO Guidelines, In: Encyclopedia of Lakes and Reservoirs, Encyclopedia of Earth Sciences Series, Springer, Dordrecht, pp. 876–883 (2012).
7. A. Rakita, N. Nikolic, M. Mildner, J. Matiasek and A. Elbe-Bürger, *Sci. Rep.*, **10**, 1 (2020); https://doi.org/10.1038/s41598-019-56847-4
8. W. Mertz, *J. Nutr.*, **123**, 626 (1993); https://doi.org/10.1093/jn/123.4.626
9. P. Kajitvichyanukul, J. Ananpattarachai and S. Pongpom, *Sci. Technol. Adv. Mater.*, **6**, 352 (2005); https://doi.org/10.1016/j.stam.2005.02.014
10. A. Hassani, L. Alidokht, A.R. Khataee and S. Karaca, *J. Taiwan Inst. Chem. Eng.*, **45**, 1597 (2014); https://doi.org/10.1016/j.jtice.2013.10.014
11. M. Arunpandian, K. Selvakumar, A. Raja, P. Rajasekaran, M. Thiruppathi, E.R. Nagarajan and S. Arunachalam, *Colloids Surf. A Physicochem. Eng. Asp.*, **567**, 213 (2019); https://doi.org/10.1016/j.colsurfa.2019.01.058
12. M.A. Omole, V.A. Okello, V. Lee, L. Zhou, O.A. Sadik, C. Umbach and B. Sammakia, *ACS Catal.*, **1**, 139 (2011); https://doi.org/10.1021/cs100034z
13. D. Park, Y.S. Yun and J.M. Park, *Environ. Sci. Technol.*, **38**, 4860 (2004); https://doi.org/10.1021/es035329+
14. R.R. Patterson, S. Fendorf and M. Fendorf, *Environ. Sci. Technol.*, **31**, 2039 (1997); https://doi.org/10.1021/es960836v
15. Z. Kalaycioglu, B. Özugur Uysal, Ö. Pekcan and F.B. Erim, *ACS Omega*, **8**, 13004 (2023); https://doi.org/10.1021/acsomega.3c00198
16. W. Chang, W. Xue, E. Liu, J. Fan and B. Zhao, *Chem. Eng. J.*, **362**, 392 (2019); https://doi.org/10.1016/j.cej.2019.01.021
17. C. Li, H. Wu, D. Zhu, T. Zhou, M. Yan, G. Chen, J. Sun, G. Dai, F. Ge and H. Dong, *Appl. Catal. B*, **297**, 120433 (2021); https://doi.org/10.1016/j.apcatb.2021.120433
18. J. Ma, K. Wang, C. Wang, X. Chen, W. Zhu, G. Zhu, W. Yao and Y. Zhu, *Appl. Catal. B*, **276**, 119150 (2020); https://doi.org/10.1016/j.apcatb.2020.119150
19. Z. Cao, Y. Jia, Q. Wang and H. Cheng, *Appl. Clay Sci.*, **212**, 106213 (2021); https://doi.org/10.1016/j.clay.2021.106213
20. D. Huang, S. Chen, G. Zeng, X. Gong, C. Zhou, M. Cheng, W. Xue, X. Yan and J. Li, *Coord. Chem. Rev.*, **385**, 44 (2019); https://doi.org/10.1016/j.ccr.2018.12.013
21. W. Zhao, Y. Li, P. Zhao, L. Zhang, B. Dai, J. Xu, H. Huang, Y. He and D.Y.C. Leung, *Chem. Eng. J.*, **405**, 126555 (2021); https://doi.org/10.1016/j.cej.2020.126555
22. J.R. Ray, X. Wu, C.W. Neil, H. Jung, Z. Li and Y.-S. Jun, *Environ. Sci.: Nano*, **6**, 2269 (2019); https://doi.org/10.1039/C9EN00201D
23. T. Munawar, F. Mukhtar, M.S. Nadeem, K. Mahmood, M. Hasan, A. Hussain, A. Ali, M.I. Arshad and F. Iqbal, *Mater. Chem. Phys.*, **253**, 123249 (2020); https://doi.org/10.1016/j.matchemphys.2020.123249
24. M.A. Subhan, A.M.M. Fahim, P.C. Saha, M.M. Rahman, K. Begum and A.K. Azad, *Nano-Struct. Nano-Objects.*, **10**, 30 (2017); https://doi.org/10.1016/j.nanoso.2017.03.001
25. A. Hezam, K. Namratha, Q.A. Drmosh, Z.H. Yamani and K. Byrappa, *Ceram. Int.*, **43**, 5292 (2017); https://doi.org/10.1016/j.ceramint.2017.01.059
26. H. Yuliani, R.D. Mayasari, E. Kalembang, Y. Deni, D.R. Santi, P.W. Pangestika, S. Purwanto, B. Sugeng, S. Suyanti and M. Setyadji, *Spektra J. Fis. Dan Apl.*, **4**, 105 (2019); https://doi.org/10.21009/SPEKTRA.043.01
27. A.V. Shishkin, V.Y. Shishkin, A.A. Maslennikova, A.B. Salyulev, P.N. Mushnikov and Y.P. Zaikov, *Processes*, **11**, 1599 (2023); https://doi.org/10.3390/pr11061599
28. H. Zhu, F. Wang, Q. Liao, Y. Wang and Y. Zhu, *Mater. Chem. Phys.*, **249**, 122936 (2020); https://doi.org/10.1016/j.matchemphys.2020.122936
29. Y. Ikuma, E. Shimada and N. Okamura, *J. Am. Ceram. Soc.*, **88**, 419 (2005); https://doi.org/10.1111/j.1551-2916.2005.00076.x
30. X. Ding, J. Ma, X. Zhou, X. Zhao, S. Hao, C. Deng and G. Li, *J. Sol-Gel Sci. Technol.*, **92**, 66 (2019); https://doi.org/10.1007/s10971-019-05058-4
31. S. Luo, F. Chai, L. Zhang, C. Wang, L. Li, X. Liu and Z. Su, *J. Mater. Chem.*, **22**, 4832 (2012); https://doi.org/10.1039/c2jm16476k
32. V. Polshettiwar, R. Luque, A. Fihri, H. Zhu, M. Bouhrara and J.M. Basset, *Chem. Rev.*, **111**, 3036 (2011); https://doi.org/10.1021/cr100230z
33. X. Yang, W. Chen, J. Huang, Y. Zhou, Y. Zhu and C. Li, *Sci. Rep.*, **5**, 10632 (2015); https://doi.org/10.1038/srep10632
34. Q. Yang, Z. Dai, K. Yang, Y. Li, Preparation of Magnetic Fe_3O_4 Microspheres Using Different Surfactant and Silica-coated Magnetic Particles, Proceedings of the AASRI International Conference on Industrial Electronics and Applications, In: Advances in Engineering Research, pp. 47-51 (2015); https://doi.org/10.2991/iea-15.2015.13
35. D.P. Ojha, M.K. Joshi and H.J. Kim, *Ceram. Int.*, **43**, 1290 (2017); https://doi.org/10.1016/j.ceramint.2016.10.079
36. C. Zou, J. Hu, Y. Su, F. Shao, Z. Tao, T. Huo, Z. Zhou, N. Hu, Z. Yang, E.S.W. Kong and Y. Zhang, *Front. Mater.*, **6**, 195 (2019); https://doi.org/10.3389/fmats.2019.00195
37. V.A. Naik and V.A. Thakur, *Inorg. Chem. Commun.*, **160**, 111962 (2024); https://doi.org/10.1016/j.inoche.2023.111962
38. D. Zhang, M.-Y. Zhu, J.-G Yu, H.-W. Meng, F.-P. Jiao, *Trans. Nonferrous Met. Soc. China*, **27**, 2673 (2017); https://doi.org/10.1016/S1003-6326(17)60296-6
39. A. Allahbakhsh, A.H. Haghighi and M. Sheydaei, *J. Therm. Anal. Calorim.*, **128**, 427 (2017); https://doi.org/10.1007/s10973-016-5915-7
40. R. Gogoi, S.K. Jena, A. Singh, K. Sharma, K. Khanna, S. Chowdhury, R. Sharma and P.F. Siril, *ChemRxiv*, (2023); https://doi.org/10.26434/chemrxiv-2023-070lf
41. U.S. Markad, A.M. Kalekar, K.K.K. Sharma, K.J. Kshirasagar, D.B. Naik and G.K. Sharma, *J. Photochem. Photobiol. Chem.*, **338**, 115 (2017); https://doi.org/10.1016/j.jphotochem.2017.01.034
42. Y. Wang, Z. Cui, G. Xiao, Y. Zhao, Y. Jin, Z. Wang, H. Su and T. Tan, *Sep. Purif. Technol.*, **227**, 115727 (2019); https://doi.org/10.1016/j.seppur.2019.115727
43. A. Bhati, S.R. Anand, D. Saini, S.K. Gunture and S.K. Sonkar, *NPJ Clean Water*, **2**, 12 (2019); https://doi.org/10.1038/s41545-019-0036-z
44. F. Liu, J. Qu, C. Yuan and G. Chen, *Mater. Res. Bull.*, **98**, 8 (2018); https://doi.org/10.1016/j.materresbull.2017.09.064
45. N. Wiriya, A. Bootchanont, S. Maensiri and E. Swatsitang, *Microelectron. Eng.*, **126**, 1 (2014); https://doi.org/10.1016/j.mee.2014.03.044
46. B. Yalcin, S. Ozcelik, K. Icin, K. Senturk, B. Ozcelik and L. Arda, *J. Mater. Sci. Mater. Electron.*, **32**, 13068 (2021); https://doi.org/10.1007/s10854-021-05752-6
47. Y. Jin, Z. Xing, Y. Li, J. Han, H. Lorenz and J. Chen, *Crystals*, **11**, 899 (2021); https://doi.org/10.3390/cryst11080899
48. S.M. Ghoreishian, K.S. Ranjith, B. Park, S.K. Hwang, R. Hosseini, R. Behjatmanesh-Ardakani, S.M. Pourmortazavi, H.U. Lee, B. Son, S. Mirsadeghi, Y.K. Han and Y.S. Huh, *Chem. Eng. J.*, **419**, 129530 (2021); https://doi.org/10.1016/j.cej.2021.129530
49. R.P. Panmand, Y.A. Sethi, R.S. Deokar, D.J. Late, H.M. Gholap, J.O. Baeg and B.B. Kale, *RSC Adv.*, **6**, 23508 (2016); https://doi.org/10.1039/C6RA01488G
50. J. Kim, V.T. Tran, S. Oh, C.-S. Kim, J.C. Hong, S.I. Kim, Y.-S. Joo, S. Mun, M.-H. Kim, J.-W. Jung, J. Lee, Y.S. Kang, J.-W. Koo and J. Lee, *ACS Appl. Mater. Interfaces*, **10**, 41935 (2018); https://doi.org/10.1021/acsami.8b14156
51. A. Szymczyk, M. Drozd, A. Kamiñska, M. Matczuk, M. Trzaskowski, M. Mazurkiewicz-Pawlicka, R. Ziólkowski and E. Malinowska, *Int. J. Mol. Sci.*, **23**, 8860 (2022); https://doi.org/10.3390/ijms23168860

52. S. Mahalingam and Y.H. Ahn, *New J. Chem.*, **42**, 4372 (2018); https://doi.org/10.1039/C8NJ00013A
53. M. Dongol, M.M. El-Nahass, A. El-Denglawey, A.F. Elhady and A.A. Abuelwafa, *Curr. Appl. Phys.*, **12**, 1178 (2012); https://doi.org/10.1016/j.cap.2012.02.051
54. Y. Liang and W. Lu, *J. Mater. Sci. Mater. Electron.*, **31**, 17075 (2020); https://doi.org/10.1007/s10854-020-04268-9
55. A.A. Ali, I.S. Ahmed and E.M. Elfiky, *J. Inorg. Organomet. Polym. Mater.*, **31**, 384 (2021); https://doi.org/10.1007/s10904-020-01695-3
56. A. Abharya and A. Gholizadeh, *Ceram. Int.*, **47**, 12010 (2021); https://doi.org/10.1016/j.ceramint.2021.01.044
57. D.S. Vavilapalli, S. Behara, R.G. Peri, T. Thomas, B. Muthuraaman, M.S.R. Rao and S. Singh, *Sci. Rep.*, **12**, 5111 (2022); https://doi.org/10.1038/s41598-022-08966-8
58. Z. Zhou, Y. Li, K. Lv, X. Wu, Q. Li and J. Luo, *Mater. Sci. Semicond. Process.*, **75**, 334 (2018); https://doi.org/10.1016/j.mssp.2017.11.011
59. J. Ouyang, Z. Zhao, S.L. Suib and H. Yang, *J. Colloid Interface Sci.*, **539**, 135 (2019); https://doi.org/10.1016/j.jcis.2018.12.052
60. E. Abdelkader, *Ceramica*, **68**, 211 (2022); https://doi.org/10.1590/0366-69132022683863228
61. C. Djebbari, E. zouaoui, N. Ammouchi, C. Nakib, D. Zouied and K. Dob, *SN Appl. Sci.*, **3**, 255 (2021); https://doi.org/10.1007/s42452-021-04266-4
62. F. Jiang, T. Yan, H. Chen, A. Sun, C. Xu and X. Wang, *Appl. Surf. Sci.*, **295**, 164 (2014); https://doi.org/10.1016/j.apsusc.2014.01.022
63. C.H. Wu and J.M. Chern, *Ind. Eng. Chem. Res.*, **45**, 6450 (2006); https://doi.org/10.1021/ie0602759
64. J.B. Islam, M. Furukawa, I. Tateishi, H. Katsumata and S. Kaneco, *Environ. Technol.*, **42**, 2740 (2021); https://doi.org/10.1080/09593330.2020.1713902
65. J. Wu, J. Wang, Y. Du, H. Li, Y. Yang and X. Jia, *Appl. Catal. B*, **174–175**, 435 (2015); https://doi.org/10.1016/j.apcatb.2015.03.040